Neutron densities from a global analysis of medium-energy proton-nucleus elastic scattering

B. C. Clark and L. J. Kerr
Department of Physics, The Ohio State University, Columbus, Ohio 43210

S. Hama
Hiroshima University of Economics, Hiroshima 731-0192, Japan
(Received 18 September 2002; published 15 May 2003)

A new method for extracting neutron densities from intermediate-energy elastic proton-nucleus scattering observables uses a global Dirac phenomenological approach based on the relativistic impulse approximation. Datasets for ^{40}Ca, ^{48}Ca, and ^{208}Pb in the energy range from 500 MeV to 1040 MeV are considered. The global fits are successful in reproducing the data and in predicting datasets not included in the analysis. Using this global approach, energy-independent neutron densities are obtained. The vector point proton density distribution ρ_v^p is determined from the empirical charge density after unfolding the proton form factor. The other densities, ρ_v^n, ρ_s^p, ρ_s^n, are parametrized. This work provides energy-independent values for the rms neutron radius R_n and the neutron skin thickness S_n, in contrast to the energy-dependent values obtained by previous studies. In addition, the results presented in this paper show that the expected rms neutron radius and the skin thickness for ^{40}Ca are accurately reproduced. The values of R_n and S_n obtained from the global fits that we consider to be the most reliable are given as follows: for ^{40}Ca, $3.314 > R_n > 3.310$ fm and $-0.063 > S_n > -0.067$ fm; for ^{48}Ca, $3.459 > R_n > 3.413$ fm and $0.102 > S_n > 0.056$ fm; and for ^{208}Pb, $5.550 > R_n > 5.522$ fm and $0.111 > S_n > 0.083$ fm. These values are in reasonable agreement with nonrelativistic Skyrme-Hartree-Fock models and with relativistic Hartree-Bogoliubov models with density-dependent meson-nucleon couplings. The results from the global fits for ^{48}Ca and ^{208}Pb are generally not in agreement with the usual relativistic mean-field models.

DOI: 10.1103/PhysRevC.67.054605 PACS number(s): 25.40.Cm, 24.10.Jv, 21.10.Gv, 24.10.Ht

I. INTRODUCTION

Determination of the proton and neutron densities, their root-mean-square radii R_p and R_n, and the neutron skin thickness $S_n = R_n - R_p$, are critical to understanding many of the bulk properties of matter [1–4]. Horowitz *et al.* have pointed out that there are substantial disagreement between theoretical values of S_n [5]. Furnstahl's recent analysis of neutron radii in the framework of mean-field models shows that relativistic mean-field models overestimate the values of S_n [6]. Parity violation electron scattering may provide the experimental data to resolve the differences in the theoretical values [7], but is also useful to have alternative methods of obtaining neutron densities. Reliable neutron densities are needed for atomic parity violation experiments [5,8–11], the analysis of antiprotonic atoms [12], in understanding the surface crust of neutron stars [13], and in extrapolation to proton-rich or neutron-rich nuclei, which is important in nuclear astrophysics [14]. In this work, we revisit the analysis of medium-energy proton-nucleus elastic scattering data with the goal of obtaining reliable, energy-independent neutron densities and the values of R_n and S_n. The analysis of elastic electron scattering, which has resulted in reliable ground state charge densities, has been a guiding light for our work [15].

For a number of years we have used the relativistic impulse approximation (RIA) in the analysis of proton-nucleus elastic and inelastic scattering [16–23] and the RIA–Kemmer-Duffin-Petiau [24–26] for meson-nucleus elastic scattering [27–31]. These approaches produce relativistic optical potentials which result in good agreement with medium-energy scattering observables. The input to these calculations are the relativistic densities from quantum hadrodynamics [32,33] and the elementary nucleon-nucleon (*NN*) amplitudes from Arndt *et al.* [34]. In recent works, we used the modern effective field theory (EFT) densities [23,30,35–37].

The seminal analysis of proton-nucleus elastic scattering data done by Ray and Hoffmann used both the RIA and the nonrelativistic KMT approach in their fits to get the observables from 300 MeV to 1040 MeV [38]. Unfortunately, neither approach produced energy-independent neutron densities. In addition, some of the values of S_n for ^{48}Ca and ^{208}Pb were negative, in contradiction to all nuclear structure calculations. Shlomo and Schaffer used the results from an analysis of 1-GeV proton elastic scattering from ^{40}Ca and ^{48}Ca to obtain the skin thickness for ^{40}Ca, ^{42}Ca, ^{44}Ca, and ^{48}Ca, see Table 2 in Ref. [39]. Starodubsky and Hintz extracted the neutron densities from elastic proton scattering of ^{206,207,208}Pb at 650 MeV and obtained S_n of (0.20 ± 0.04) fm for ^{208}Pb [40]. However, the energy independence of the neutron densities in the work of Ref. [39] or Ref. [40] was not addressed. Recently, Karataglidis *et al.* have calculated proton and neutron elastic scattering from ^{208}Pb and ^{40}Ca targets at three energies 40 MeV, 65 MeV, and 200 MeV. They used a model based on coordinate space nonlocal optical potentials using the full folding *NN* interactions with various Skyrme model ground-state densities [42]. For ^{208}Pb they found that the SKM* model gave the best agreement with proton and neutron elastic scattering data at 40 MeV, 65 MeV, and 200 MeV. Based on this, the authors

suggest that S_n for ^{40}Ca is ~ -0.05 fm, and for ^{208}Pb it is ~ 0.17 fm [41].

In this paper, a new analysis of proton-nucleus elastic scattering is used to obtain the neutron density. This work is motivated by our considerable experience in obtaining high quality global proton-nucleus optical potentials from 20 MeV to 1040 MeV [44]. The new method meshes the global approach with the RIA and proves to be successful in obtaining energy-independent neutron densities. The starting point is the RIA in its simplest form, which for spin-zero nuclei includes only scalar, vector, and tensor terms. The tensor term is very small and is excluded; as was done in the RIA analysis done by Ray and Hoffmann [38].

We find that substantial progress in extracting the neutron densities from proton-nucleus elastic scattering is made by using a global approach focusing on the energy region where the RIA is capable of reproducing experiment very well. We have obtained values of S_n for ^{40}Ca, ^{48}Ca, and ^{208}Pb, which agree with nonrelativistic Skyrme models [1,42,43] and relativistic Hartree-Bogoliubov model extended to include density-dependent meson-nucleon couplings [4]. Our results for ^{48}Ca and ^{208}Pb are generally not in agreement with relativistic mean-field model, see Ref. [6] and references therein.

The organization of this paper is as follows. Section II describes the global method to obtain the neutron density. Section III discusses the results and the sensitivity of the extracted neutron density, R_n and S_n, to the input used in the fitting procedure. The values of S_n and the neutron rms radii R_n for ^{40}Ca, ^{48}Ca, and ^{208}Pb for the various tests of the input to the model are given in this section. The summary and conclusions are presented in Sec. IV.

II. RIA GLOBAL METHOD FOR EXTRACTING THE NEUTRON DENSITY

The RIA nuclear reaction formalism is used as the basis of global fits to medium-energy proton-nucleus elastic scattering data. The input to the RIA consists of the Arndt *NN* amplitudes [34] and the point proton density, which is fixed from the charge distribution obtained from electron-nucleus scattering. The neutron vector density, and the scalar proton and neutron densities are parametrized, resulting in good fits of $p+A$ elastic scattering data between 500 MeV and 1040 MeV. Using the RIA as the basis for the global fits is a new approach, and our results shows that it is a valid method for extracting neutron densities, R_n and S_n.

In the global approach used in this work, the form of the RIA vector, scalar, and tensor optical potentials are given by

$$U_s(r) = -\frac{P_{lab}}{(2\pi)^2 m} \times \sum_{j=p,n} \int_0^{\bar{q}} 4\pi q^2 dq \frac{R(q)}{R(0)} j_0(qr) F_s^j(q) \tilde{\rho}_s^j(q), \tag{1}$$

$$U_v(r) = -\frac{P_{lab}}{(2\pi)^2 m} \times \sum_{j=p,n} \int_0^{\bar{q}} 4\pi q^2 dq \frac{R(q)}{R(0)} j_0(qr) F_v^j(q) \tilde{\rho}_v^j(q), \tag{2}$$

$$U_t(r) = -\frac{P_{lab}}{(2\pi)^2 m} \times \sum_{j=p,n} \left[r \int_0^{\bar{q}} 4\pi q^2 dq \frac{R(q)}{R(0)} j_0(qr) F_t^j(q) \tilde{\rho}_t^j(q) + \int_0^{\bar{q}} 4\pi q^2 dq \frac{d}{dq}\left(\frac{R(q)}{R(0)} F_t^j(q) \right) j_1(qr) \tilde{\rho}_t^j(q) \right], \tag{3}$$

where the Fourier transforms of the density form factors are

$$\tilde{\rho}_s^j(q) = \int d^3r' e^{i\vec{q}\cdot\vec{r}'} \rho_s^j(r'), \tag{4}$$

$$\tilde{\rho}_v^j(q) = \int d^3r' e^{i\vec{q}\cdot\vec{r}'} \rho_v^j(r'), \tag{5}$$

$$\tilde{\rho}_t^j(q) = \int d^3r' e^{i\vec{q}\cdot\vec{r}'} \frac{1}{r'} \rho_t^j(r'). \tag{6}$$

The subscripts s,v,t refer to Lorentz scalar, vector (timelike), and tensor quantities. The superscripts n and p refer to neutrons and protons, $F(q)$ are the invariant *NN* amplitudes, and $R(q)$ is the kinematical factor required to obtain the invariant *NN* amplitude in the Breit frame [38]. The value of the upper limit on the momentum transfer $\bar{q}$ is determined by the available on-shell *NN* data. Many studies conducted have demonstrated that higher order corrections to this first-order RIA-Dirac optical model approach are negligible at the energies being studied in this paper. See Ray *et al.* for more details of the RIA-Dirac calculations used for elastic scattering observables [16].

Elastic $p+A$ data between 500 MeV and 1040 MeV for ^{40}Ca, ^{48}Ca, and ^{208}Pb form the dataset. The quality of the fits are good, and the predictions of data not in the dataset is used to verify the procedure. However, unlike the usual RIA, where we have generally used scalar, vector, and tensor densities from the results of relativistic EFT calculations, we use the RIA as a basis for extracting the vector neutron density as well as the two scalar densities using a global fitting procedure.

Next we describe the treatment of the vector and scalar densities. The point proton density is fixed by using the results from electron scattering as follows:

$$\rho_v^p(r) = \frac{1}{(2\pi)^3} \int d^3q e^{-i\vec{q}\cdot\vec{r}} \tilde{\rho}_v^p(q), \tag{7}$$

where

$$\tilde{\rho}_v^p(q) = \frac{\int d^3q e^{i\vec{q}\cdot\vec{r}}\rho_c(r)}{G(q)}. \quad (8)$$

Here $\rho_c(r)$ is the experimental charge density and $G(q)$ is the proton form factor. The point proton density $\rho_v^p(r)$ is normalized to Z and the neutron density $\rho_v^n(r)$ is normalized to N.

The next step is to consider the model that will be used. After several years of testing a number of different forms used to parametrize the neutron vector and scalar densities, we have chosen to model the vector neutron density and the scalar proton and neutron densities using the cosh form used in many of our global fits [44]. We have found that the cosh form parametrization produced more stable results for R_n and S_n than the three-parameter Fermi (3PF) or the sum of Gaussian (SOG) parametrizations. This stability of the cosh was understood from the results from many global fits using all the three forms. In global fits we used four or five different momentum transfer ranges. For example, if five momentum transfer ranges are used, the fits are done from 0.0 fm^{-1}–1.5 fm^{-1} to 0.0 fm^{-1}–3.5 fm^{-1} in steps of 0.5 fm^{-1}. In future work we will consider other parametrizations.

In the form of the cosh model in this work, the superscript V stands for volume and S for surface terms,

$$f^V(r,R,a) = \frac{\{\cosh[R/a]-1\}}{\{\cosh[R/a]+\cosh[r/a]-2\}}, \quad (9)$$

$$f^S(r,R,a) = \frac{\{\cosh[R/a]-1\}\{\cosh[r/a]-1\}}{\{\cosh[R/a]+\cosh[r/a]-2\}^2}. \quad (10)$$

The vector neutron density is

$$\rho_v^n(r,R_b,a_b) = \rho^B(r,R_b,a_b) - \rho_v^p(r). \quad (11)$$

The density $\rho^B(r,R_b,a_b)$ is given by

$$\rho^B(r,R_b,a_b) \propto f^V(r,R_b,a_b) + \alpha f^S(r,R_b,a_b), \quad (12)$$

and $\rho^B(r,R_b,a_b)$ is normalized to A. There are two geometric parameters R_b and a_b, and the parameter α.

The scalar proton and neutron densities are

$$\rho_s^p(r,R_s^p,a_s^p) \propto f^V(r,R_s^p,a_s^p) + \beta f^S(r,R_s^p,a_s^p) \quad (13)$$

and

$$\rho_s^n(r,R_s^n,a_s^n) \propto f^V(r,R_s^n,a_s^n) + \gamma f^S(r,R_s^n,a_s^n). \quad (14)$$

Each of these densities contains three parameters, two geometry parameters, R_b^p, R_b^n, a_b^p, a_b^n, and the parameters β and γ. The tenth parameter searched, P_{10}, is given by $\int d^3r\rho_s^p = P_{10}\,Z$. A similar 11th parameter given by $\int d^3r\rho_s^n = P_{11}\,N$ could also have been searched. However, the searches were more stable if the ratio $(\int d^3r\rho_s^p/Z)/(\int d^3r\rho_s^n/N)$, i.e., the ratio of P_{10}/P_{11}, was fixed by ratio of the volume integrals per particle of the scalar proton and neutron densities from any one of the EFT models given by Rusnak and co-workers [36,37]. Three different EFT densities are used, two are point coupling models, VA3 and FZ4, and one is a meson model, MA4. The parameter P_{10} is not sensitive to the EFT model chosen, and the final difference and the scalar proton and neutron densities are not sensitive to the EFT model chosen, even though the values of S_n for $N \neq Z$ in these models differ widely. For example, values of S_n for ^{208}Pb are 0.332 fm for VA3, 0.259 fm for MA4, and 0.160 fm for FZ4.

As mentioned above, we found that the model used in this paper was the best of many different models we tried. We will investigate other models in future work using this global approach.

III. FITTING PROCEDURE AND RESULTS

It has long been known that using a global approach has been very useful in obtaining *NN* amplitudes and the *NN* phase shifts. This is one of the reasons for using a global approach when the dataset used is large and usually correlated. In this work we use elastic $p+A$ data between 500 MeV and 1040 MeV for ^{40}Ca, ^{48}Ca, and ^{208}Pb. For ^{40}Ca there are five energies; 497.5 MeV [45,46], 613 MeV [47], 650 MeV [48], 797.5 MeV [49,50], and 1040 MeV [51,52]. For ^{208}Pb there are five energies; 497.5 MeV [45,53], 613 MeV [47], 650 MeV [54,55], 797.5 MeV [56,57], and 1040 MeV [58]. However, for ^{48}Ca only three energies (497.5 MeV [45], 797.5 MeV [59], and 1044 MeV [51,52]) are available. In order to make predictions of data not included in the dataset, we remove one energy. For ^{40}Ca and ^{208}Pb, the 650-MeV data have been excluded; and for ^{48}Ca, 1044-MeV data have been excluded. The quality of the global fits to the data are good, and the predictions for data not in the global datasets verify the procedure.

In previous Dirac phenomenology work global fitting, the datasets were cut at 100 degrees in the center of mass or at momentum transfer q at 3.0 fm^{-1}, whichever came first. In this work we do global fits using a variety of momentum transfer values as discussed below. In addition, as is discussed later, we also test the sensitivity of the input to the model.

In the global fitting, we have used five momentum transfer ranges from 0.0 fm^{-1}–1.5 fm^{-1} to 0.0 fm^{-1}–3.5 fm^{-1} in steps of 0.5 fm^{-1}; or four momentum transfer ranges from 0.0 fm^{-1}–2.0 fm^{-1} to 0.0 fm^{-1}–3.5 fm^{-1}, again in steps of 0.5 fm^{-1}. The values of S_n and R_n are expected to change with the value of the momentum transfer range used as the datasets are changed. We find that the values of S_n and R_n for a given momentum transfer range (we use five momentum transfer ranges or four momentum transfer ranges) are clustered in a reasonably well-constrained set of values for S_n and R_n, we call these stable results. The momentum transfer range for 0.0–1.5 fm^{-1} is almost always the outlier, which is understandable as the dataset is small and does not have the diffraction structure needed when fitting proton scattering from nuclear targets. Of course, in any such global approach the datasets are usually correlated. This is certainly true as the datasets sets with different momentum transfer ranges do overlap. Thus a statistical analysis to obtain a

mean value and a standard deviation cannot generally be used. However, we can determine the range of the values of S_n and R_n for each fit from every momentum transfer range, and obtain the values for S_n and R_n which could be shown as a scatter plot, as is usually done when datasets used are correlated. We have obtained the range of values for S_n and R_n for every test considered, while these ranges cannot be interpreted as resulting from a statistical analysis; we found that doing such an analysis gives a useful guide to present the results.

There are a number of features in the fitting procedures which could produce changes in the neutron density, R_n and S_n. As mentioned above, two ranges of momentum transfer cuts are used. In the following sensitivity tests, we use both ranges. Generally, the smaller range produces the smallest range of values for R_n and S_n, so in most of the figures we show the larger range values for R_n and S_n, which gives the most conservative results.

We test the results obtained when the following features of the model used in the fitting procedures are changed. First, the three different EFT models used in fixing the tenth parameter are considered [36,37]. To investigate the effect of the $G(q)$ used in obtaining the point proton density, we use two different forms; they are identified as $G_1(q)$ from Ref. [60] and $G_2(q)$ from Ref. [61]. The set chosen for the Arndt *NN* amplitudes is input to the fitting procedure, and we use sets FA00 and SM86 to find the sensitivity of the fits to this input [34]. The datasets included in the fits have been changed to see if the results change significantly. Finally, we use the three different charge density models used in the analysis of electron-nucleus elastic scattering data; the 3PF, the SOG, and the Fourier-Bessel (FB) model [62]. Thus for each target we have done global fits that have used effective field theory densities MA4, FZ4, and VA3, and for each three, charge distributions are used. In addition, two different form factors $G_1(q)$ and $G_2(q)$ and two sets of Arndt amplitudes are used, sets FA00 and SM86. Figures 1–5 show the results of these tests of the global fitting procedure. The results for the R_n and S_n are given in the three tables; Table I for ^{40}Ca, Table II for ^{48}Ca, and Table III for ^{208}Pb.

There are three general cases used in testing the global fits: case 1 uses the Arndt amplitude set FA00 and the $G_1(q)$ form factor; case 2 uses the Arndt amplitude set FA00 and the $G_2(q)$ form factor; and case 3 uses the Arndt amplitude set SM86 and the $G_1(q)$ form factor. In every case, we obtain good global fits for MA4, FZ4, and VA3 for every charge distribution used; SOG, 3PF, and FB. As discussed above, the momentum cut ranges used are 0.0 fm^{-1}–1.5 fm^{-1} to 0.0 fm^{-1}–3.5 fm^{-1} in steps of 0.5 fm^{-1}, or we remove the 0.0 fm^{-1}–1.5 fm^{-1} set. For each case, for the one with five momentum transfer ranges or four momentum transfer ranges, we calculate the mean and standard deviation for R_n and S_n for every global fit; this gives us an average over all EFT models for a given charge distribution. This is denoted by AVE_{EFT} in the tables. This is not to be taken as a statistical error; it is, however, a convenient way to show the range of the values in a consistent way. We do this rather than removing every outlier. Then for each case we show the combined values of the range for R_n and S_n for that case, this gives the average over all charge distributions as well as over all EFT models. These results are denoted as AVE_{CD} and AVE_{EFT} in the tables. Finally, we calculate the ranges of R_n and S_n for all three cases combined for each target.

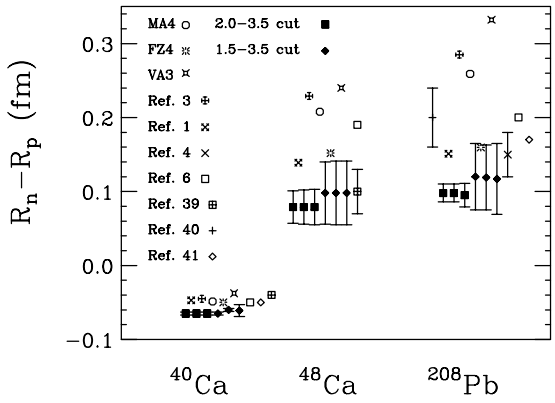

FIG. 1. The ranges, shown as bars, of the skin thickness for ^{40}Ca, ^{48}Ca, and ^{208}Pb from the global fits using the SOG charge distribution, the set FA00 Arndt *NN* amplitudes, the proton form factor $G_1(q)$, and the three EFT models MA4, FZ4 and VA3 are shown by the filled boxes for the four momentum transfer ranges and the filled diamonds for the five momentum transfer ranges. Several theoretical S_n values from Refs. [1,3,4,6,36,37,39–41] are also shown by using various symbols.

The last calculation, which combines all of the values of R_n and S_n for every test made, gives us the most conservative results. From these final test cases, shown at the bottom of the tables, we get the following values using the five momentum transfer ranges: for ^{40}Ca, $3.350 > R_n > 3.300$ fm and $-0.008 > S_n > -0.080$ fm; and for ^{48}Ca, $3.505 > R_n > 3.421$ fm and $0.148 > S_n > 0.058$ fm; for ^{208}Pb, $5.589 > R_n > 5.513$ fm and $0.156 > S_n > 0.076$ fm. As mentioned earlier, if we use the four momentum transfer ranges, results are generally more clustered, and we obtain: for ^{40}Ca,

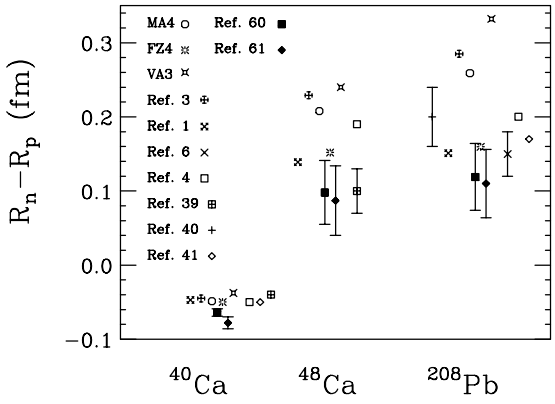

FIG. 2. The skin thickness with different proton form factors. Results for ^{40}Ca, ^{48}Ca, and ^{208}Pb from the global fitting procedure shows the AVE_{EFT} model values for the SOG charge distribution, the set FA00 Arndt *NN* amplitudes, and the five momentum transfer ranges. We compare $G_1(q)$ from Ref. [60] shown as filled boxes and $G_2(q)$ from Ref. [61] shown as filled diamonds. The same theoretical values for S_n shown in Fig. 1 are also shown.

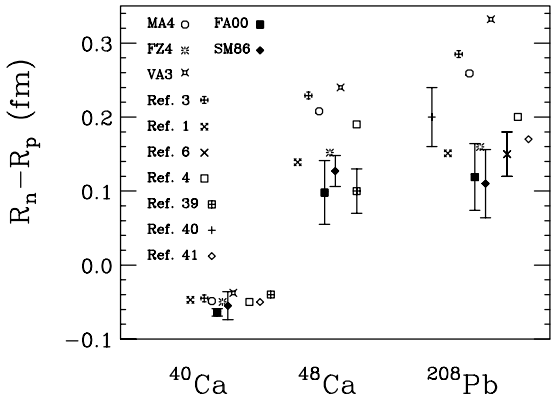

FIG. 3. The skin thickness for ^{40}Ca, ^{48}Ca, and ^{208}Pb due to different sets of Arndt *NN* amplitudes. The global results shown are the AVE_{EFT} models for SOG charge distribution, the five momentum transfer ranges, and proton form factor $G_1(q)$. The set FA00 is shown as filled boxes and the set SM86 is shown as filled diamonds. The same theoretical values for S_n shown in Fig. 1 are also shown.

$3.350 > R_n > 3.304$ fm and $-0.006 > S_n > -0.080$ fm; for ^{48}Ca, $3.485 > R_n > 3.417$ fm and $0.129 > S_n > 0.053$ fm; and for ^{208}Pb, $5.561 > R_n > 5.513$ fm and $0.130 > S_n > 0.074$ fm. The values for R_n and S_n for both of the final case results are quite similar.

However, the authors found that the global fits using the Arndt *NN* amplitude set FA00 and the form factor $G_1(q)$ gave the most stable results i.e., the values did not vary very much, see Tables I–III. This is especially true for using the SOG charge distribution. In this case the values of R_n and S_n using the five momentum transfer ranges are: for ^{40}Ca, $3.318 > R_n > 3.308$ fm and $-0.059 > S_n > -0.069$ fm; for ^{48}Ca, $3.498 > R_n > 3.412$ fm and $0.141 > S_n > 0.055$ fm; and

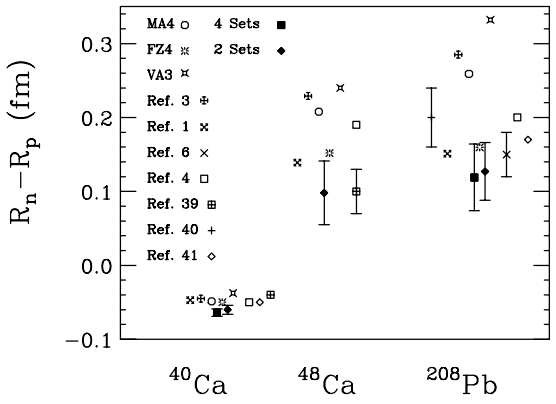

FIG. 4. The skin thickness for ^{40}Ca, ^{48}Ca, and ^{208}Pb when different datasets included in the fits; one has four energies and the other has two energies. The results of the global procedure use the AVE_{EFT} models, the SOG charge distribution, the five momentum transfer ranges, the proton form factor $G_1(q)$, and the set FA00 Arndt *NN* amplitudes. The results for four-energy sets are shown by filled boxes and the results for two-energy datasets by filled diamonds. The dataset for ^{48}Ca has only three energies, so only two datasets are used in the fits. The same theoretical values for S_n shown in Fig. 1 are also shown.

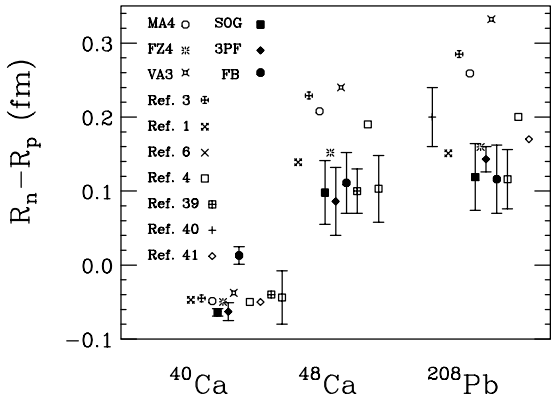

FIG. 5. The figure shows the change in the skin thickness for ^{40}Ca, ^{48}Ca, and ^{208}Pb due to different charge distribution models. The global fits use the set FA00 Arndt *NN* amplitudes, the five momentum transfer ranges, and the proton from factor $G_1(q)$. The results for the AVE_{EFT} SOG are shown by filled boxes, the AVE_{EFT} 3PF are shown by filled diamonds, and the AVE_{EFT} FB are shown by filled circles. The results for all effective field theory cases and for all three charge distributions, i.e., the results from the final cases are given by the open squares. The same theoretical values for S_n shown in Fig. 1 are also shown.

for ^{208}Pb, $5.602 > R_n > 5.512$ fm and $0.164 > S_n > 0.074$ fm. The values for R_n and S_n using the four-momentum transfer ranges are: for ^{40}Ca, $3.314 > R_n > 3.310$ fm and $-0.063 > S_n > -0.067$ fm; for ^{48}Ca, $3.459 > R_n > 3.413$ fm and $0.102 > S_n > 0.056$ fm; and for ^{208}Pb, $5.550 > R_n > 5.522$ fm and $0.111 > S_n > 0.083$ fm.

The results using the form factor $G_2(q)$ are quite similar, as well as the case using the form factor $G_1(q)$ but with the *NN* set SM86. These values as well as the values obtained from the final case values are in agreement with nonrelativistic Skyrme models [1,42,43], the relativistic Hartree-Bogoliubov model extended to include density-dependent meson-nucleon couplings [4], and the recent analysis of antiproton atoms [12]. Our results are generally not in agreement with relativistic mean-field models.

Next we discuss the results of each test of the model separately. Figure 1 shows the effect of the two different momentum transfer ranges as well as the difference in the three EFT models used to fix parameter (10). The filled boxes (the smaller momentum transfer range) and diamonds (the larger momentum transfer range) are the values from the three different EFT models used. The charge density used in this case was the SOG for all targets, the proton form factor $G_1(q)$, and the set FA00 Arndt *NN* amplitudes. This figure shows that the results from the two different momentum ranges overlap and that the EFT model used does not affect the results. The figure also shows several theoretical results from Refs. [1,3,4,6,36,37,39–41]. The comparison between theory and range of the values from the fits shows that all theoretical S_n values agree with the results of the global fits for ^{40}Ca. However, the theoretical S_n values for ^{48}Ca and ^{208}Pb are somewhat larger than the global fits.

Next we consider the results when two different proton form factors, $G_1(q)$ from Ref. [60] and $G_2(q)$ from Ref. [61], are used in obtaining the vector point proton density for

TABLE I. R_n and S_n for ^{40}Ca.

Range (fm^{-1})	R_n (fm)	S_n (fm)
	^{40}Ca (case 1)	
	$G_1(q)$	FA00
	SOG	AVE_{EFT}
2.0–3.5	$3.314 > R_n > 3.310$	$-0.063 > S_n > -0.067$
1.5–3.5	$3.318 > R_n > 3.308$	$-0.059 > S_n > -0.069$
	3PF	AVE_{EFT}
2.0–3.5	$3.328 > R_n > 3.304$	$-0.051 > S_n > -0.075$
1.5–3.5	$3.328 > R_n > 3.304$	$-0.051 > S_n > -0.075$
	FB	AVE_{EFT}
2.0–3.5	$3.373 > R_n > 3.349$	$0.028 > S_n > 0.004$
1.5–3.5	$3.371 > R_n > 3.347$	$0.025 > S_n > 0.001$
	AVE_{CD}	AVE_{EFT}
2.0–3.5	$3.354 > R_n > 3.306$	$0.002 > S_n > -0.076$
1.5–3.5	$3.352 > R_n > 3.306$	$0.000 > S_n > -0.076$
	^{40}Ca (case 2)	
	$G_2(q)$	FA00
	SOG	AVE_{EFT}
2.0–3.5	$3.314 > R_n > 3.300$	$-0.070 > S_n > -0.084$
1.5–3.5	$3.315 > R_n > 3.299$	$-0.069 > S_n > -0.085$
	3PF	AVE_{EFT}
2.0–3.5	$3.317 > R_n > 3.299$	$-0.070 > S_n > -0.088$
1.5–3.5	$3.324 > R_n > 3.296$	$-0.062 > S_n > -0.090$
	FB	AVE_{EFT}
2.0–3.5	$3.341 > R_n > 3.333$	$-0.012 > S_n > -0.020$
1.5–3.5	$3.340 > R_n > 3.332$	$-0.013 > S_n > -0.021$
	AVE_{CD}	AVE_{EFT}
2.0–3.5	$3.333 > R_n > 3.301$	$-0.027 > S_n > -0.087$
1.5–3.5	$3.334 > R_n > 3.302$	$-0.026 > S_n > -0.086$
	^{40}Ca (case 3)	
	$G_1(q)$	SM86
	SOG	AVE_{EFT}
2.0–3.5	$3.344 > R_n > 3.308$	$-0.033 > S_n > -0.069$
1.5–3.5	$3.341 > R_n > 3.305$	$-0.036 > S_n > -0.072$
	3PF	AVE_{EFT}
2.0–3.5	$3.332 > R_n > 3.302$	$-0.047 > S_n > -0.077$
1.5–3.5	$3.330 > R_n > 3.292$	$-0.049 > S_n > -0.087$
	FB	AVE_{EFT}
2.0–3.5	$3.374 > R_n > 3.340$	$0.028 > S_n > -0.006$
1.5–3.5	$3.371 > R_n > 3.335$	$0.025 > S_n > -0.011$
	AVE_{CD}	AVE_{EFT}
2.0–3.5	$3.356 > R_n > 3.308$	$0.002 > S_n > -0.070$
1.5–3.5	$3.354 > R_n > 3.304$	$-0.001 > S_n > -0.075$
	^{40}Ca (for all three cases)	
2.0–3.5	$3.350 > R_n > 3.304$	$-0.006 > S_n > -0.080$
1.5–3.5	$3.350 > R_n > 3.300$	$-0.008 > S_n > -0.080$

TABLE II. R_n and S_n for ^{48}Ca.

Range (fm^{-1})	R_n (fm)	S_n (fm)
	^{48}Ca (case 1)	
	$G_1(q)$	FA00
	SOG	AVE_{EFT}
2.0–3.5	$3.459 > R_n > 3.413$	$0.102 > S_n > 0.056$
1.5–3.5	$3.498 > R_n > 3.412$	$0.141 > S_n > 0.055$
	3PF	AVE_{EFT}
2.0–3.5	$3.456 > R_n > 3.412$	$0.087 > S_n > 0.043$
1.5–3.5	$3.501 > R_n > 3.409$	$0.132 > S_n > 0.040$
	FB	AVE_{EFT}
2.0–3.5	$3.460 > R_n > 3.420$	$0.113 > S_n > 0.073$
1.5–3.5	$3.499 > R_n > 3.417$	$0.152 > S_n > 0.070$
	AVE_{CD}	AVE_{EFT}
2.0–3.5	$3.459 > R_n > 3.415$	$0.103 > S_n > 0.055$
1.5–3.5	$3.499 > R_n > 3.413$	$0.142 > S_n > 0.054$
	^{48}Ca (case 2)	
	$G_2(q)$	FA00
	SOG	AVE_{EFT}
2.0–3.5	$3.453 > R_n > 3.407$	$0.089 > S_n > 0.043$
1.5–3.5	$3.498 > R_n > 3.404$	$0.134 > S_n > 0.040$
	3PF	AVE_{EFT}
2.0–3.5	$3.448 > R_n > 3.404$	$0.072 > S_n > 0.028$
1.5–3.5	$3.500 > R_n > 3.398$	$0.124 > S_n > 0.022$
	FB	AVE_{EFT}
2.0–3.5	$3.458 > R_n > 3.414$	$0.103 > S_n > 0.059$
1.5–3.5	$3.511 > R_n > 3.407$	$0.157 > S_n > 0.053$
	AVE_{CD}	AVE_{EFT}
2.0–3.5	$3.454 > R_n > 3.408$	$0.092 > S_n > 0.040$
1.5–3.5	$3.503 > R_n > 3.403$	$0.139 > S_n > 0.037$
	^{48}Ca (case 3)	
	$G_1(q)$	SM86
	SOG	AVE_{EFT}
2.0–3.5	$3.506 > R_n > 3.476$	$0.150 > S_n > 0.120$
1.5–3.5	$3.505 > R_n > 3.463$	$0.148 > S_n > 0.106$
	3PF	AVE_{EFT}
2.0–3.5	$3.487 > R_n > 3.447$	$0.119 > S_n > 0.079$
1.5–3.5	$3.484 > R_n > 3.446$	$0.116 > S_n > 0.078$
	FB	AVE_{EFT}
2.0–3.5	$3.516 > R_n > 3.486$	$0.169 > S_n > 0.139$
1.5–3.5	$3.515 > R_n > 3.473$	$0.167 > S_n > 0.125$
	AVE_{CD}	AVE_{EFT}
2.0–3.5	$3.509 > R_n > 3.465$	$0.158 > S_n > 0.100$
1.5–3.5	$3.504 > R_n > 3.458$	$0.152 > S_n > 0.094$
	^{48}Ca (for all three cases)	
2.0–3.5	$3.485 > R_n > 3.417$	$0.129 > S_n > 0.053$
1.5–3.5	$3.505 > R_n > 3.421$	$0.148 > S_n > 0.058$

a given charge distribution model. The five momentum transfer ranges, the values for the AVE_{EFT} models for the SOG model charge distribution, and the set FA00 Arndt *NN* amplitudes are used and shown in Fig. 2.

Investigating the sensitivity to the set of the Arndt *NN* amplitudes used is done by comparing the sets FA00 and SM86. The larger momentum transfer range, the averaged EFT models for the SOG model charge distribution, and the proton form factor $G_1(q)$ are used and shown in Fig. 3.

In order to check the sensitivity due to the datasets included in the fit, we have done fits using only two datasets (497.5 MeV and 797.5 MeV) for ^{40}Ca and ^{208}Pb. The results agree very well with the same case using four datasets, as is shown in Fig. 4. The values of S_n for the two-dataset case are

TABLE III. R_n and S_n for ^{208}Pb.

Range (fm^{-1})	R_n (fm)	S_n (fm)
	^{208}Pb (case 1)	
	$G_1(q)$	FA00
	SOG	AVE_{EFT}
2.0–3.5	$5.550>R_n>5.522$	$0.111>S_n>0.083$
1.5–3.5	$5.602>R_n>5.512$	$0.164>S_n>0.074$
	3PF	AVE_{EFT}
2.0–3.5	$5.580>R_n>5.548$	$0.155>S_n>0.123$
1.5–3.5	$5.586>R_n>5.552$	$0.160>S_n>0.126$
	FB	AVE_{EFT}
2.0–3.5	$5.546>R_n>5.518$	$0.108>S_n>0.080$
1.5–3.5	$5.600>R_n>5.508$	$0.162>S_n>0.070$
	AVE_{CD}	AVE_{EFT}
2.0–3.5	$5.565>R_n>5.523$	$0.135>S_n>0.085$
1.5–3.5	$5.599>R_n>5.521$	$0.167>S_n>0.085$
	^{208}Pb (case 2)	
	$G_2(q)$	FA00
	SOG	AVE_{EFT}
2.0–3.5	$5.545>R_n>5.517$	$0.102>S_n>0.074$
1.5–3.5	$5.599>R_n>5.507$	$0.156>S_n>0.064$
	3PF	AVE_{EFT}
2.0–3.5	$5.576>R_n>5.538$	$0.146>S_n>0.108$
1.5–3.5	$5.582>R_n>5.542$	$0.152>S_n>0.112$
	FB	AVE_{EFT}
2.0–3.5	$5.537>R_n>5.511$	$0.095>S_n>0.069$
1.5–3.5	$5.593>R_n>5.499$	$0.151>S_n>0.057$
	AVE_{CD}	AVE_{EFT}
2.0–3.5	$5.558>R_n>5.516$	$0.124>S_n>0.074$
1.5–3.5	$5.594>R_n>5.514$	$0.157>S_n>0.075$
	^{208}Pb (case 3)	
	$G_1(q)$	SM86
	SOG	AVE_{EFT}
2.0–3.5	$5.538>R_n>5.498$	$0.100>S_n>0.060$
1.5–3.5	$5.554>R_n>5.502$	$0.115>S_n>0.063$
	3PF	AVE_{EFT}
2.0–3.5	$5.584>R_n>5.532$	$0.158>S_n>0.106$
1.5–3.5	$5.590>R_n>5.538$	$0.165>S_n>0.113$
	FB	AVE_{EFT}
2.0–3.5	$5.532>R_n>5.502$	$0.094>S_n>0.064$
1.5–3.5	$5.551>R_n>5.503$	$0.113>S_n>0.065$
	AVE_{CD}	AVE_{EFT}
2.0–3.5	$5.559>R_n>5.503$	$0.129>S_n>0.065$
1.5–3.5	$5.571>R_n>5.509$	$0.141>S_n>0.071$
	^{208}Pb (for all three cases)	
2.0–3.5	$5.561>R_n>5.513$	$0.130>S_n>0.074$
1.5–3.5	$5.589>R_n>5.513$	$0.156>S_n>0.076$

for ^{40}Ca ($-0.054>S_n>-0.066$ fm) and for ^{208}Pb ($0.166>S_n>0.088$ fm). These results agree very well with the values for the four-dataset case for ^{40}Ca ($-0.059>S_n>-0.069$ fm) and for ^{208}Pb ($0.164>S_n>0.074$ fm). This encourages us to extend our global procedure to nuclei that have at least two datasets in the medium-energy range.

The sensitivity of S_n and R_n to the three different charge distributions 3PF, SOG, and FB obtained from Ref. [62] (which are used in the fitting procedure) is shown in Fig. 5 and given in detail in Tables I–III. The five momentum transfer ranges, the proton form factor $G_1(q)$, and the set FA00 Arndt *NN* amplitudes are used. For ^{208}Pb and ^{48}Ca, there is little difference in the values of S_n and R_n for the different charge densities. We note that the rms radii for ^{208}Pb and ^{48}Ca for these three charge densities are almost the same [62]. Two of the three ^{40}Ca charge distributions also have almost identical charge rms radii, 3PF of 3.482(25) fm and SOG of and 3.479(3)fm, but the rms radius for the FB [3.450(10) fm] is considerably smaller (see Ref. [62]). The result is that for ^{40}Ca the difference in the value of S_n is pronounced. As shown in Fig. 5, the FB charge distribution has a range of S_n values which goes from positive to negative, but the range of the S_n values 3PF and SOG are all negative. We attribute this to the smaller rms radius for the FB charge distribution. The values of R_p, R_n, and S_n should not depend heavily on the momentum transfer ranges, the set of amplitudes, the form factors, and the charge distribution. In fact, the only case that does not overlap is the FB case for ^{40}Ca. The results for all three of the charge distributions are given in Tables I–III.

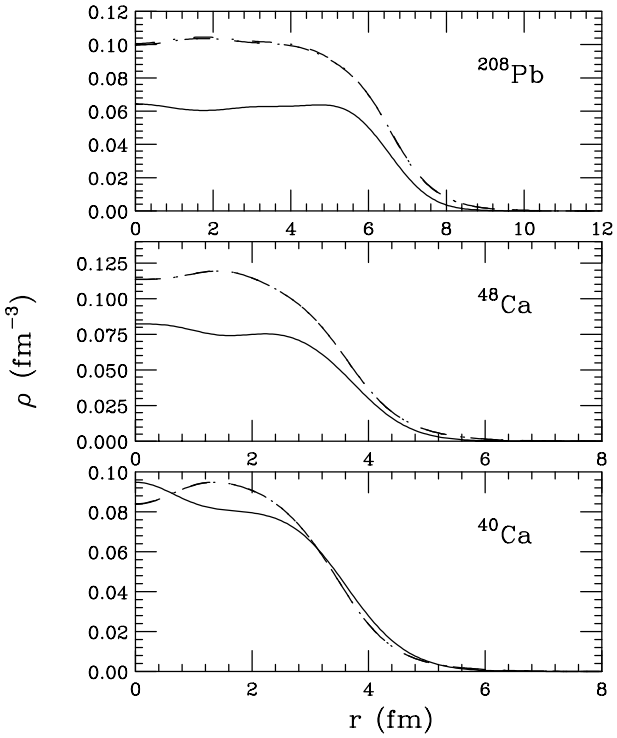

FIG. 6. The vector point proton density distribution shown by the solid curve. The three neutron density distribution densities using the EFT densities, MA4, FZ4, and VA3 are shown by the dashed line for the case MA4, by the dots for the case FZ4, and by dot dashes for the case VA3. All densities are obtained from the global fit as discussed in the paper.

In this global analysis, we obtain many densities from the various cases used in checking the results of the fits. Figures 6 and 7 show the vector point proton density distributions ρ_v^p

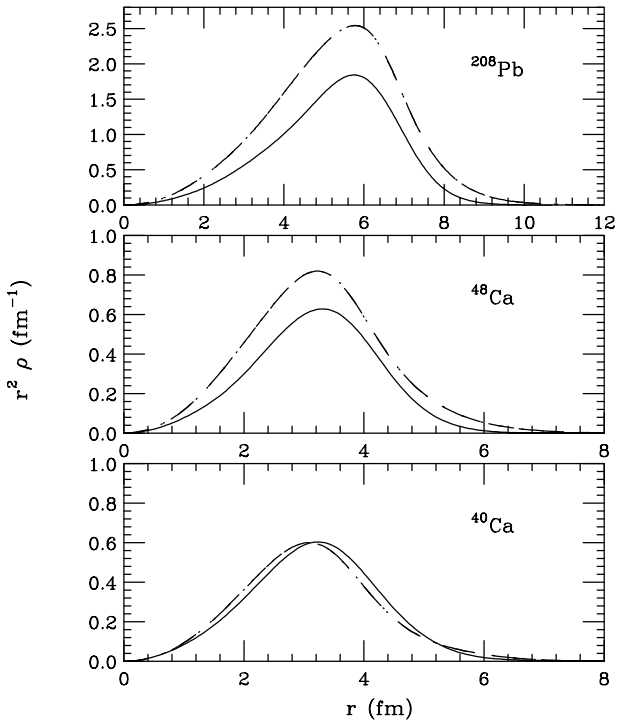

FIG. 7. The vector point proton density distribution shown by the solid curve. The three neutron density distribution densities using the EFT densities MA4, FZ4, and VA3 are shown by the dashed line for the case MA4, by the dots for the case FZ4, and by dot dashes for the case VA3. All densities are multiplied by the radius squared, and obtained from the global fit as discussed in the paper.

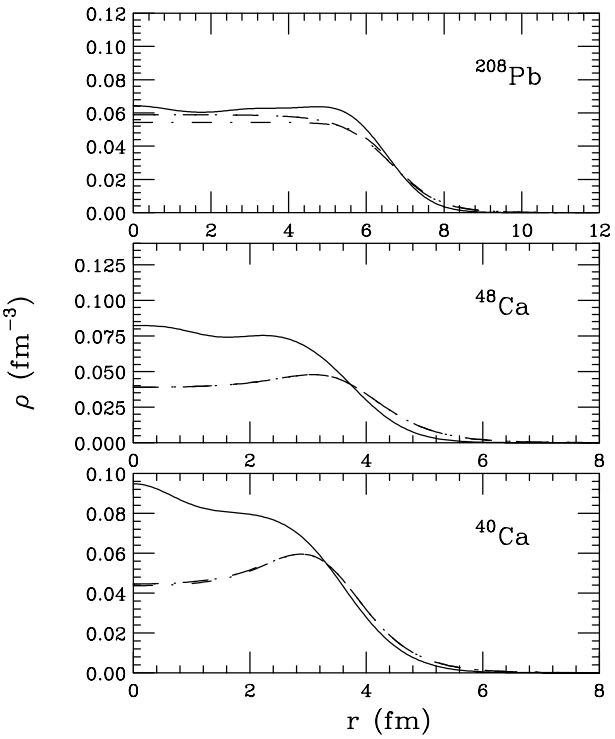

FIG. 8. The vector point proton density distribution shown by the solid curve. The three scalar proton density distribution densities using the EFT densities MA4, FZ4, and VA3 are shown by the dashed line for the case MA4, the dots for the case FZ4, and dot dashes for the case VA3. All densities are obtained from the global fit as discussed in the paper.

and $r^2\rho_v^p$ and the vector point neutron density distribution, ρ_v^n and $r^2\rho_v^n$ for ^{40}Ca, ^{48}Ca, and ^{208}Pb. The SOG charge distribution and the $G_1(q)$ form factor were used to obtain the vector point proton density. The neutron density also depends on the charge distribution chosen and the form factor used to obtain the vector point proton density as well as the other input to a given global fit, the *NN* amplitudes, and the EFT density used to fix the ratio of P_{10}/P_{11}. In Figs. 6 and 7 the Arndt *NN* amplitude set FA00, the SOG charge distribution, the momentum transfer range of 0.0–3.0 fm^{-1}, the proton form factor $G_1(q)$, and all three EFT cases (MA4, FZ4, and VA3) are used. It is clear that the neutron densities overlap, showing that the use of different EFT cases does not have any significant impact on the global fit. Tables of the densities and the parameters are available from Ref. [63].

These same inputs as in Figs. 6 and 7 are also used in Figs. 8 and 9 that show the vector proton point density and the scalar proton (ρ_s^p and $r^2\rho_s^p$), and in Figs. 10 and 11 for the vector point density and the scalar neutron (ρ_s^n and $r^2\rho_s^n$). Figures 8–11 show that the phenomenology gives sensible scalar densities that are not unphysical.

Figures 12 and 13 show the observables for one of the energies included in the global fit for ^{40}Ca, and a prediction of an energy not included in the global fit. Figure 12 shows the fit for ^{40}Ca at 497.5 MeV, and Fig. 13 shows the prediction for the ^{40}Ca 650 MeV spin observables; no cross section data are available. Figures 14 and 15 show the observables for one of the energies included in the global fit for ^{48}Ca and the results from a prediction of an energy not included in the global fit. Figure 14 shows the fit for ^{48}Ca at 497.5 MeV and the prediction of Q at that energy. Figure 15 shows the prediction for ^{48}Ca at 1044 MeV. Figures 16 and 17 show the observables for one of the energies included in the global fit for ^{208}Pb and the results from a prediction of an energy not included in the global fit. Figure 16 shows the fit for ^{208}Pb at 497.5 MeV, and Fig. 17 shows the prediction for the 650 MeV observables for this target. All the observables shown in Figs. 12–17 used the Arndt *NN* amplitude set FA00, the SOG charge distribution, the proton from factor $G_1(q)$, the momentum transfer range from 0.0 fm^{-1} to 3.0 fm^{-1}, and the EFT case MA4.

While the figures of the observable are small, we have magnified them and we find that the heights of the diffractive maxima and the angular positions of the minima and maxima are very well reproduced at each energy, with no systematic energy-dependent discrepancies. These are the most critical features of the data, which determine the rms radii. In fact, precision fits to A_y and Q are not as important for determining neutron radii, but our fits are quite reasonable. The magnified figures are available from Refs. [63].

We also predict the total neutron cross section and the proton reaction cross section. In Fig. 18 the predicted total neutron cross sections for ^{40}Ca and ^{208}Pb are compared with the experimental values from Finlay *et al.* [64]. The predicted proton reaction cross sections for the same two targets

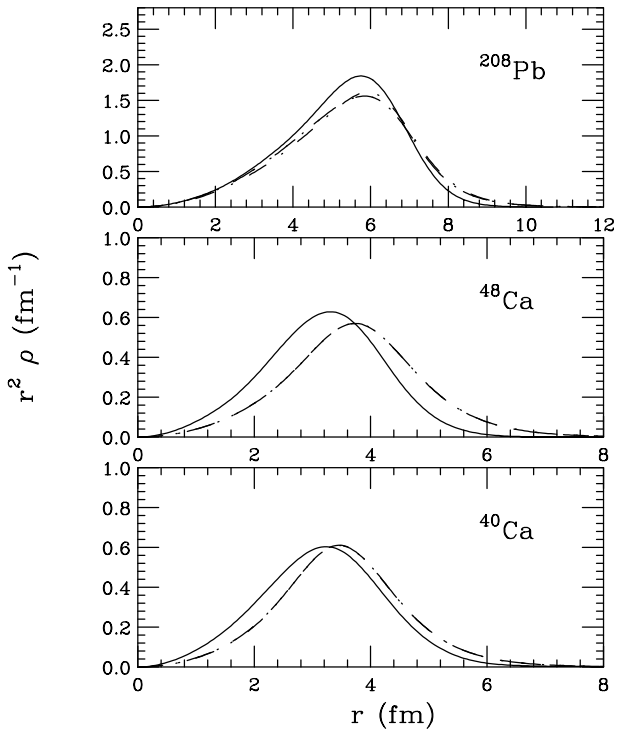

FIG. 9. The vector point proton density distribution shown by the solid curve. The three scalar proton density distribution densities using the EFT densities MA4, FZ4, and VA3 are shown by the dashed line for the case MA4, the dots for the case FZ4, and dot dashes for the case VA3. All densities are multiplied by the radius squared and obtained from the global fit as discussed in the paper.

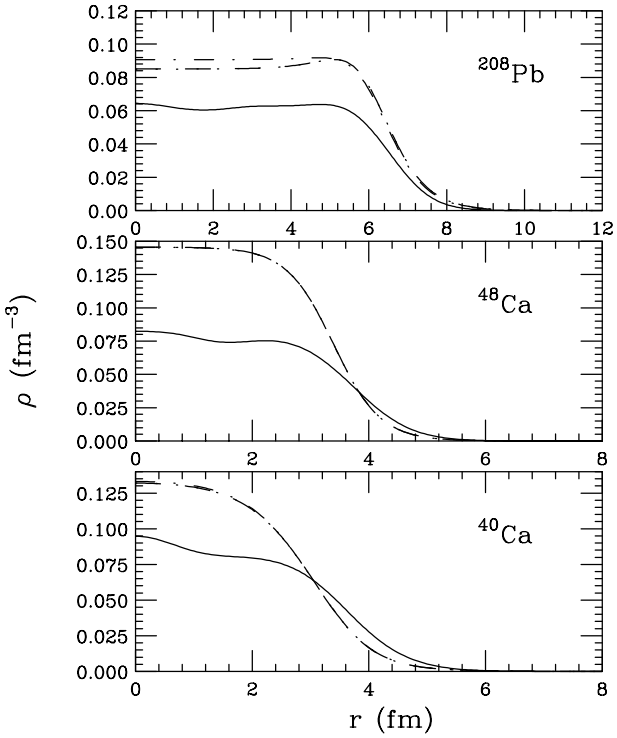

FIG. 10. The vector point proton density distribution shown by the solid curve. The three neutron scalar density distribution densities using the EFT densities MA4, FZ4, and VA3 are shown by the dashed line for case MA4, the dots for the case FZ4, and dot dashes for the case VA3. All densities are obtained from the global fit as discussed in the paper.

are given in Fig. 19 with the experimental values [65], and the predictions are reasonable.

All of the results confirm that the global approach produces good fits to the data, that predictions are quite acceptable, and that the neutron densities are energy independent. These densities will prove to be a useful input to a large number of nuclear reactions. They provide the empirical values of R_n and S_n, which are needed for testing theoretical models.

IV. SUMMARY AND CONCLUSIONS

This paper reports on a new method for extracting neutron densities from intermediate-energy elastic proton-nucleus scattering observables. Neutron densities are needed for atomic parity violation experiments, the analysis of antiproton atoms, the experiments parity violation elastic electron scattering, and theoretical nonrelativistic and covariant mean-field models. It is interesting to note that our results for S_n are in agreement with the work using antiprotonic atoms, see Fig. 4 in Ref. [12].

The approach uses a global analysis, similar to the global fits using Dirac phenomenology, but in this case it is based on the relativistic impulse approximation (RIA). The input to the procedure are the vector point proton density distribution ρ_v^p that is determined from the empirical charge density after unfolding the proton form factor and the Arndt *NN* amplitudes. The other densities (ρ_v^n, ρ_s^p, ρ_s^n), are parametrized. The neutron densities for ^{40}Ca, ^{48}Ca, and ^{208}Pb obtained from the global fits have been tested for sensitivity to the input. Different proton form factors, different charge densities, different sets of the Arndt *NN* amplitudes, different EFT models, different datasets included in the fits, and differences in the ranges of the momentum transfer used in the fits have been investigated. With the exception of the Fourier-Bessel charge density for ^{40}Ca, all of these tests produce values for R_n and S_n, which overlap. The prediction of datasets not used in the fits are well reproduced, and the calculated observables are in good agreement with data.

In conclusion, we have obtained values of R_n and S_n for ^{40}Ca, ^{48}Ca, and ^{208}Pb. We have obtained good global fits for MA4, FZ4, and VA3 for every charge distribution used; SOG, 3PF, and FB. Both five momentum transfer ranges and four momentum transfer ranges were used. As discussed earlier, for each case we calculate the mean and standard deviation for R_n and S_n for every global fit, this gives us an average over all EFT models for a given charge distribution. This is denoted by AVE_{EFT} in the tables. As mentioned several times, this is not to be taken as a statistical analysis; but as a way to show the range of the values in a consistent way, they are shown as bars in the figures. We do this rather than removing the outliers. Then for each case we show the combined values of the range for R_n and S_n for that case, this gives the average over all charge distributions as well as over all EFT models. These results are denoted as AVE_{CD} and

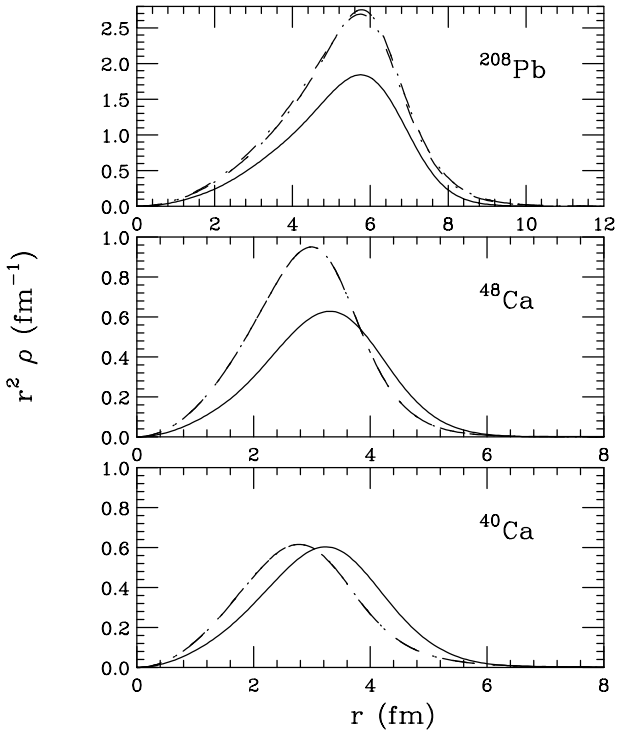

FIG. 11. The vector point proton density distribution shown by the solid curve. The three neutron scalar density distribution densities using the EFT densities MA4, FZ4, and VA3 are shown by the dashed line for the case MA4, the dots for the case FZ4, and dot dashes for the case VA3. All densities are multiplied by the radius squared and obtained from the global fit as discussed in the paper.

AVE_{EFT} in the tables. We then calculate the ranges of R_n and S_n for all three cases combined for each target. From these final test cases, shown at the bottom of the tables, using the five momentum transfer ranges we obtain the following values: for ^{40}Ca, $3.350 > R_n > 3.300$ fm and $-0.008 > S_n > -0.080$ fm; for ^{48}Ca, $3.505 > R_n > 3.421$ fm and $0.148 > S_n > 0.058$ fm; and for ^{208}Pb, $5.589 > R_n > 5.513$ and $0.156 > S_n > 0.076$ fm. In conclusion, the rms neutron radius R_n and the neutron skin thickness S_n obtained from the global fits that we consider to be the most reliable ranges of our results are given as follows: for ^{40}Ca, $3.314 > R_n > 3.310$ fm and $-0.063 > S_n > -0.067$ fm; for ^{48}Ca, $3.459 > R_n > 3.413$ fm and $0.102 > S_n > 0.056$ fm; and for ^{208}Pb, $5.550 > R_n > 5.522$ fm and $0.111 > S_n > 0.083$ fm.

The authors have found that the global fits are more stable when using the Arndt *NN* amplitude set FA00 rather than the Arndt *NN* amplitude set SM86. This might be expected as

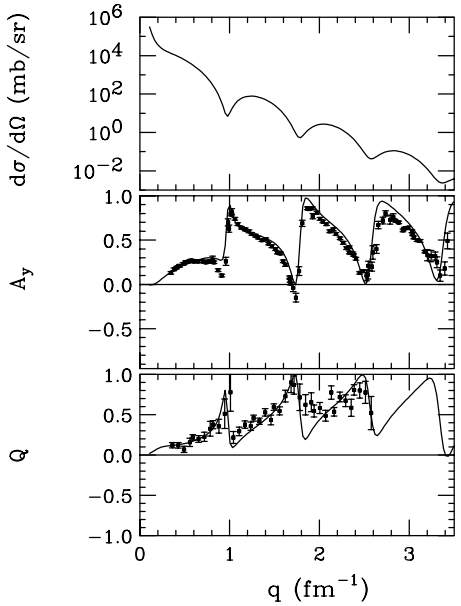

FIG. 13. Prediction for ^{40}Ca at 650 MeV.

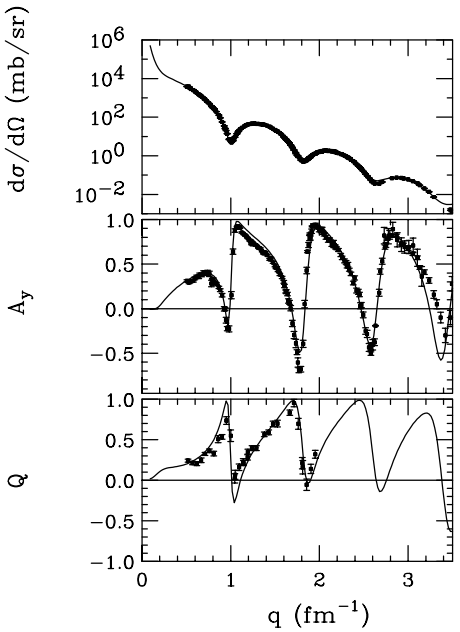

FIG. 12. Results of the global analysis for ^{40}Ca at 497.5 MeV.

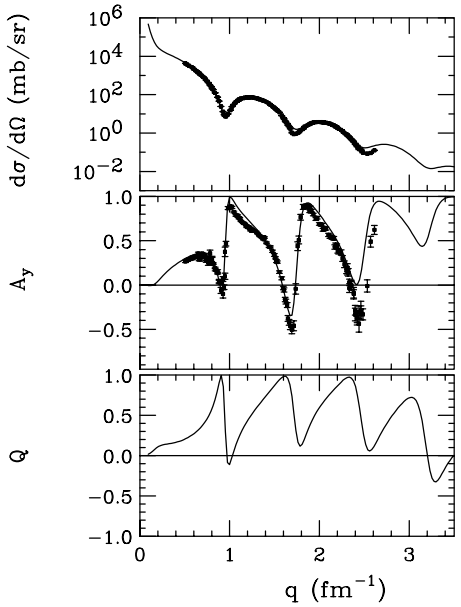

FIG. 14. Results of the global analysis for ^{48}Ca at 497.5 MeV.

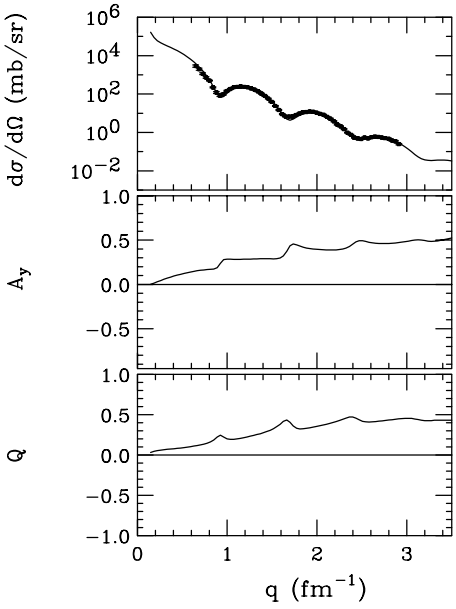

FIG. 15. Prediction for ^{48}Ca at 1044 MeV.

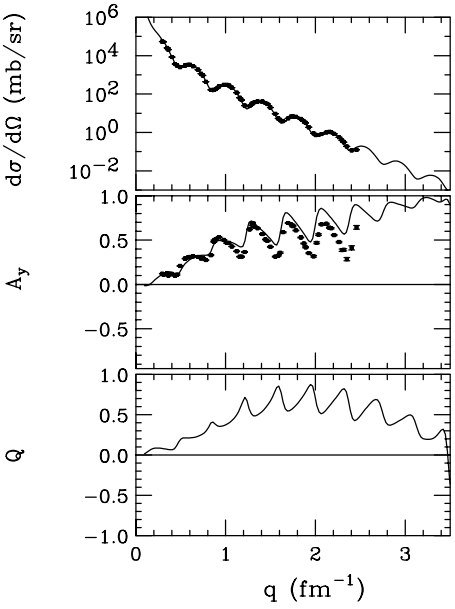

FIG. 17. Prediction for ^{208}Pb at 650 MeV.

the FA00 analysis is more recent. Both of the form factors were used, $G_1(q)$ and $G_2(q)$, when using FA00 were the most stable, see Tables I–III. The impact on the fits due to the charge distribution inputs SOG, 3PF, and FB, as shown in Fig. 5, clearly showed that the cases using the SOG and 3PF charge distributions were stable, i.e., the ranges overlapped for all targets. However, for ^{40}Ca the results for the FB charge distribution gave very different results, see Table I. We also found that the fits using the Arndt *NN* amplitude set FA00, the $G_1(q)$ form factor, and the SOG charge distribution produced the most stable results. In this case the values of R_n and S_n using the five momentum transfer ranges are: for ^{40}Ca, $3.318 > R_n > 3.308$ fm and $-0.059 > S_n > -0.069$ fm; for ^{48}Ca, $3.498 > R_n > 3.412$ fm and $0.141 > S_n > 0.055$ fm; and for ^{208}Pb, $5.602 > R_n > 5.512$ fm and $0.164 > S_n > 0.074$ fm. These values, as well as the values using the most conservative errors and the results that we consider most reliable, are in agreement with nonrelativistic Skyrme models [1,42,43], relativistic Hartree-Bogoliubov model extended to include density-dependent meson-nucleon

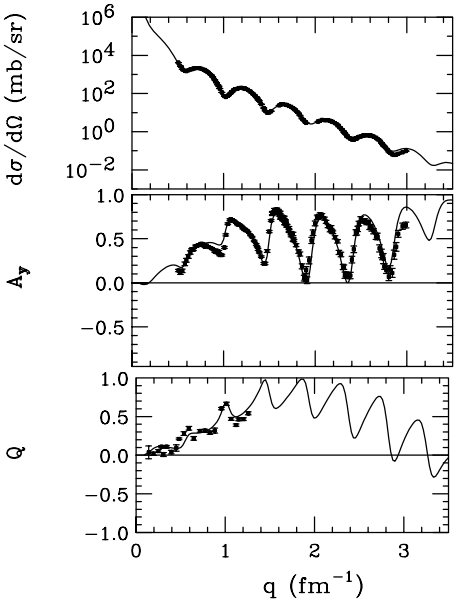

FIG. 16. Results of the global analysis for ^{208}Pb at 497.5 MeV.

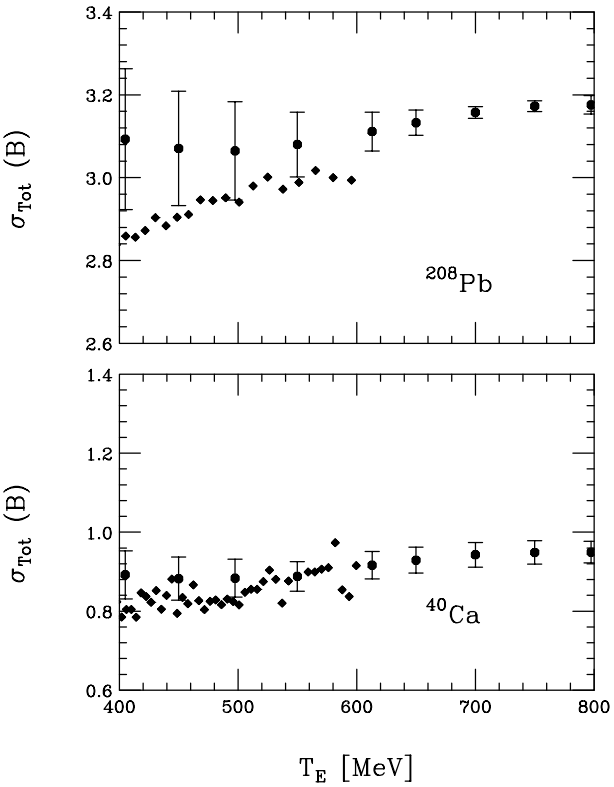

FIG. 18. Predicted total cross sections for ^{40}Ca and ^{208}Pb shown as circles are compared with the experimental values (shown as diamonds) from Ref. [64].

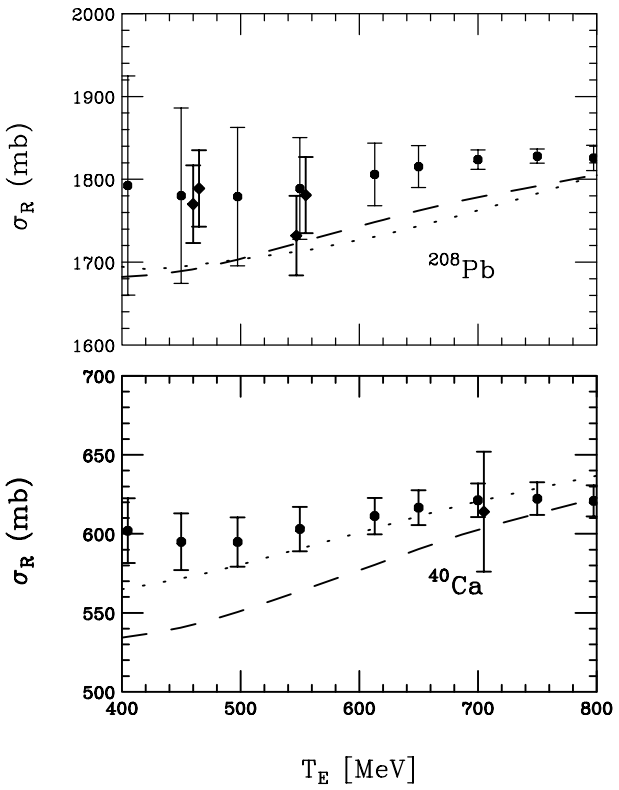

FIG. 19. Predicted proton reaction cross sections are shown as circles for ^{40}Ca and ^{208}Pb, compared with the experimental values (shown as diamonds) from Ref. [65]. The dashed lines are the results of the EDAI global fit and the dotted lines are the EDAD fit (3) from Ref. [44].

couplings [4], and results from a recent analysis of antiprotonic atoms [12]. Our results for ^{48}Ca and ^{208}Pb are generally not in agreement with relativistic mean-field models, see Ref. [6] and references therein.

The global fit based on the RIA is a new tool for obtaining the neutron density. The values of R_n and S_n obtained are robust. This quality is verified in several ways as discussed in Sec. III. For example, we checked the sensitivity due to the datasets included in the fit by doing global fits using only two datasets (497.5 MeV and 797.5 MeV) for ^{40}Ca and ^{208}Pb, as well as four datasets. The values of S_n for the two-dataset case are: for ^{40}Ca, $-0.054 > S_n > -0.066$ fm; and for ^{208}Pb, $0.166 > S_n > 0.088$ fm. These results agree well with S_n for the four-dataset case: for ^{40}Ca, $-0.059 > S_n > -0.069$ fm; and for ^{208}Pb, $0.164 > S_n > 0.074$ fm. These results, shown in Fig. 4, motivate us to use the global procedure for all nuclei that have at least two datasets in the medium-energy range.

This work provides energy-independent values for R_n and S_n, in contrast to the energy-dependent values obtained by previous studies. In addition, the results presented in this paper show that the expected rms neutron radius and skin thickness for ^{40}Ca are accurately reproduced. The values of R_n and S_n obtained from the global fits that we consider to be the most reliable are given as follows. We plan to extend our work to additional nuclei and will continue to investigate different models and procedures. The goal is to continue to improve quality of neutron densities that result from our global fits.

ACKNOWLEDGMENTS

We thank R. J. Furnstahl, C. J. Horowitz, L. Ray, and B. D. Serot for useful discussions. S.H. also thanks the Department of Physics, The Ohio State University, for their support for a part of this work. B.C.C. and S.H. thank the National Institute for Nuclear Theory for their hospitality. This work was supported in part by the National Science Foundation under Grant Nos. PHY-9800964 and PHY-0098645.

[1] B.A. Brown, Phys. Rev. C **58**, 220 (1998), and references therein.
[2] P. Ring, Prog. Part. Nucl. Phys. **37**, 193 (1996), and references therein.
[3] K. Pomorski *et al.*, Nucl. Phys. **A624**, 349 (1997).
[4] T. Nikšić, D. Vretenar, P. Finelli, and P. Ring, nucl-th/0205009.
[5] C.J. Horowitz, S.J. Pollock, P.A. Souder, and R. Michaels, Phys. Rev. C **63**, 025501 (2001).
[6] R.J. Furnstahl, Nucl. Phys. **A709**, 85 (2002).
[7] R. Michaels, P. A. Souder, and G. M. Urciuoli, Jefferson Laboratory Report No. E-00-003.
[8] E.N. Fortson, Y. Pang, and L. Wilets, Phys. Rev. Lett. **65**, 2857 (1990).
[9] S.J. Pollock, E.N. Fortson, and L. Wilets, Phys. Rev. C **46**, 2587 (1992).
[10] B.Q. Chen and P. Vogel, Phys. Rev. C **48**, 1392 (1993).
[11] S.J. Pollock and M.C. Welliver, Phys. Lett. B **464**, 177 (1999).
[12] A. Trzcinska *et al.*, Phys. Rev. Lett. **87**, 082501 (2002).
[13] C.J. Horowitz and J. Piekarewicz, Phys. Rev. Lett. **86**, 5647 (2001).
[14] R. Casten *et al.*, Report from the Nuclear Structure and Astrophysics Town Meeting, 2000 (unpublished).
[15] B. Frois *et al.*, Phys. Rev. Lett. **38**, 152 (1977).
[16] L. Ray, G.W. Hoffmann, and W.R. Coker, Phys. Rep. **212**, 223 (1992), and references therein.
[17] S. Shim, B.C. Clark, S. Hama, E.D. Cooper, R.L. Mercer, L. Ray, and G.W. Hoffmann, Phys. Rev. C **38**, 1968 (1988).
[18] S. Shim, Ph.D. thesis, The Ohio State University, 1989.
[19] S. Shim, B.C. Clark, E.D. Cooper, S. Hama, R.L. Mercer, L. Ray, J. Raynal, and H.S. Sherif, Phys. Rev. C **42**, 1592 (1990).
[20] L. Kurth, B.C. Clark, E.D. Cooper, S. Hama, S. Shim, R.L. Mercer, L. Ray, and G.W. Hoffmann, Phys. Rev. C **49**, 2086 (1994), and references therein.
[21] S. Shim, M.W. Kim, B.C. Clark, and L. Kurth Kerr, Phys. Rev. C **59**, 317 (1999).
[22] S. Shim, B.C. Clark, and L. Kurth Kerr, Phys. Rev. C **62**, 067602 (2000).
[23] B. C. Clark, S. Hama, and L. Kerr (unpublished).
[24] N. Kemmer, Proc. R. Soc. London, Ser. A **173**, 91 (1939).

[25] R.J. Duffin, Phys. Rev. **54**, 1114 (1938).
[26] G. Petiau, Acad. Roy. Belg. Cl. Sci. Mom. Collect. **16**, 6 (1936).
[27] B.C. Clark, S. Hama, G.R. Kälbermann, R.L. Mercer, and L. Ray, Phys. Rev. Lett. **55**, 592 (1985), and references therein.
[28] L.J. Kurth, B.C. Clark, E.D. Cooper, S. Hama, R.L. Mercer, L. Ray, and G.W. Hoffmann, Phys. Rev. C **50**, 2624 (1994).
[29] George Kahrimanis *et al.*, Phys. Rev. C **55**, 2533 (1997).
[30] B.C. Clark, R.J. Furnstahl, L. Kurth-Kerr, John Rusnak, and S. Hama, Phys. Lett. B **427**, 231 (1998).
[31] L. Kurth-Kerr, B.C. Clark, S. Hama, L. Ray, and G.W. Hoffmann, Prog. Theor. Phys. **103**, 321 (2000).
[32] B.D. Serot and J.D. Walecka, Adv. Nucl. Phys. **16**, 1 (1986).
[33] B.D. Serot, Rep. Prog. **55**, 1855 (1992).
[34] R.A. Arndt, J.S. Hyslop, and L.D. Roper, Phys. Rev. D **35**, 128 (1987); Richard A. Arndt, Igor I. Strakovsky, Ron L. Workman, and Marcello M. Pavan, Phys. Rev. C **52**, 2120 (1995); R. A. Arndt (private communication).
[35] R.J. Furnstahl, B.D. Serot, and H.-B. Tang, Nucl. Phys. **A615**, 441 (1997).
[36] J.J. Rusnak and R.J. Furnstahl, Nucl. Phys. **A627**, 495 (1997).
[37] John J. Rusnak, Ph.D. thesis, Ohio State University, 1997.
[38] L. Ray and G.W. Hoffmann, Phys. Rev. C **31**, 538 (1985).
[39] S. Shlomo and R. Schaeffer, Phys. Lett. **83B**, 5 (1979).
[40] V.E. Starodubsky and N.M. Hintz, Phys. Rev. C **49**, 2118 (1994).
[41] S. Karataglidis, K. Amos, B.A. Brown, and P.K. Deb, Phys. Rev. C **65**, 044306 (2002); (private communication).
[42] B. Alex Brown, Phys. Rev. Lett. **85**, 5296 (2000).
[43] S. Typel and B. Alex Brown, Phys. Rev. C **64**, 027302 (2001).
[44] E.D. Cooper, S. Hama, B.C. Clark, and R.L. Mercer, Phys. Rev. C **47**, 297 (1993), and references therein.
[45] G.W. Hoffmann *et al.*, Phys. Rev. Lett. **47**, 1436 (1981).
[46] A. Rahbar *et al.*, Phys. Rev. Lett. **47**, 1811 (1981).
[47] G. Burge, Report No. DPh-N/78-1, 1978 (unpublished).
[48] E. Belszynski *et al.*, Phys. Rev. C **37**, 1527 (1988).
[49] L. Ray *et al.*, Phys. Rev. C **23**, 828 (1981).
[50] R.W. Fergerson *et al.*, Phys. Rev. C **33**, 239 (1986).
[51] G.D. Alkhazov *et al.*, Phys. Lett. **90B**, 364 (1980).
[52] G.D. Alkhazov *et al.*, Nucl. Phys. **A274**, 443 (1976).
[53] B. Aas *et al.*, Nucl. Phys. **A460**, 675 (1986).
[54] N. M. Hintz *et al.* (unpublished).
[55] A. M. Mack *et al.* (unpublished).
[56] G.W. Hoffmann *et al.*, Phys. Rev. C **21**, 1488 (1980).
[57] G.W. Hoffmann *et al.*, Phys. Rev. C **24**, 541 (1981).
[58] R. Bertini *et al.*, Phys. Lett. **45B**, 119 (1973).
[59] G. Igo *et al.*, Phys. Lett. **81B**, 1511 (1979).
[60] G.H. Höhler *et al.*, Nucl. Phys. **B114**, 505 (1976).
[61] R.B. Wiringa, V.G.J. Stoks, and R. Schiavilla, Phys. Rev. C **51**, 38 (1995).
[62] H. De Vries, C.W. De Jager, and C. De Vries, At. Data Nucl. Data Tables **36**, 495 (1987).
[63] Contact B.C. Clark, Clark.36@osu.edu, to get tables of the densities and parameters obtained from the fits. Magnified plots of the observables are also available from B.C. Clark.
[64] R.W. Finlay *et al.*, Phys. Rev. C **47**, 237 (1993).
[65] W. Baufoff, At. Data Nucl. Data Tables **35**, 429 (1986).